

## The Guderley problem revisited

Scott D. Ramsey<sup>a\*</sup>, James R. Kamm<sup>b</sup> and John H. Bolstad<sup>c</sup>

<sup>a</sup>Los Alamos National Laboratory, X-Computational Physics Division, Los Alamos, NM 87545, USA; <sup>b</sup>Sandia National Laboratories, Albuquerque, NM 87185, USA; <sup>c</sup>Consultant, Livermore, CA 94550, USA

(Received 4 May 2011; final version received 29 November 2011)

The self-similar converging-diverging shock wave problem introduced by Guderley in 1942 has been the source of considerable mathematical and physical interest. We investigate a novel application of the Guderley solution as a unique and challenging code verification test problem for compressible flow algorithms; this effort requires a unified understanding of the problem's mathematical and computational subtleties. Hence, we review the simplifications and group invariance properties that reduce the compressible flow equations for a polytropic gas to two coupled nonlinear eigenvalue problems: the first for the similarity exponent in the converging regime, and the second for a trajectory multiplier in the diverging regime. The information we provide, together with previously published material, gives a complete description of the computational steps required to construct a semi-analytic Guderley solution. We employ the problem in a quantitative code verification analysis of a cell-centred, finite volume, Eulerian compressible flow algorithm. Lastly, in appended material, we introduce a new approximation for the similarity exponent, which may prove useful in the future construction of certain semi-analytic Guderley solutions.

**Keywords:** compressible flow; shock waves; exact fluid flow solution; convergent flow; code verification

### 1. Introduction

The problem of a strong shock wave converging cylindrically or spherically in a gas is well known in hydrodynamics and is considered important in varied contexts. For example, the problem of converging compressible flow is familiar to the laser fusion community (Motz 1979, Atzeni and Meyer-ter-Vehn 2004, Clark and Tabak 2006, Rygg 2006) and in astrophysical contexts, e.g. with relevance to double-detonation supernovae (Fink *et al.* 2007).

Guderley (1942) was the first to investigate the basic problem of a strong cylindrically or spherically symmetric shock wave converging into an inviscid, non-radiating, non-heat-conducting, perfect gas (though this particular problem was also solved independently by Landau and Stanyukovich (Stanyukovich 1970) in 1944). Guderley recognised that certain physical assumptions lead to a self-similar problem formulation. The solution of the self-similar problem is contingent upon the determination of the numerical value of a so-called 'similarity exponent' that characterises the space–time path of the infinite-strength incoming (converging) and finite-strength reflected (diverging) shock waves in proximity to the location of collapse. In the years following Guderley's seminal work, various authors including Butler (1954), Lazarus and Richtmyer (1977), Lazarus (1981) and

Hafner (1998) calculated the numerical value of this similarity exponent (a function of the adiabatic exponent and geometry) to several significant figures using various techniques.

The 'classic' Guderley problem, also reviewed by Meyer-ter-Vehn and Schalk (1982), Zel'dovich and Raizer (2002) and Sachdev (2004), has variations that have been explored in some detail. Axford and Holm (1978) used group theoretic techniques to determine a more general equation of state (represented through the adiabatic bulk modulus) that admits self-similar solutions for a Guderley-type problem. Wu and Roberts (1996) investigated the special case of a strong shock wave converging into a Van der Waals gas, and various authors have found similarity solutions for strong shock waves converging into dusty gases (Jena and Sharma 1999), variable-density gases (Toqué 2001, Madhumita and Sharma 2003), and radiating gases (NiCastro 1970, Hirschler 2002). In addition, Axford and Holm (1981) explored a quasi-self-similar solution regime for finite-strength shocks, Ponchaut *et al.* (Ponchaut 2005, Ponchaut *et al.* 2006) also relaxed Guderley's original strong shock assumption, and Hornung *et al.* (2008) considered the universality of imploding shock solutions from examination of approximate solutions for the Guderley problem and computed solutions of converging shocked flows.

\*Corresponding author. Email: ramsey@lanl.gov

The stability of Guderley flows was first investigated by Morawetz (1951) and subsequently discussed by Häfele (1956), Axford and Holm (1978), Brushlinskii (1982) and Clarisse (2007).

Consistent with the assumptions motivating the governing Euler equations of inviscid, non-heat-conducting, compressible flow, the converging shock wave reflects through the origin, resulting in a diverging shock wave immediately following focus. It is easily proven that the similarity exponent governing the trajectory of the reflected shock is the same as that determined for the incoming case; consequently, many authors do not address reflection. Some authors, such as Fernández (1977), Lazarus and Richtmyer (1977), Rodríguez and Amable (1978), Lazarus (1981), Bilbao and Gratton (1996), Wu and Roberts (1996), and Ponchaut (2005), engage in discussions describing the flow into and out of the reflected shock wave.

In fact, the reflected portion of Guderley's converging shock wave problem constitutes a separate eigenvalue problem. In addition to the similarity exponent determined as part of the analysis of the converging portion, an *a priori* unknown trajectory multiplier must be determined in order to fully realise the (scale-invariant) physical flow variables. This multiplier is determined numerically through integration of the reduced flow equations on either side of the reflected shock, supplemented by boundary condition matching; this is achieved through the satisfaction of the generalised Rankine-Hugoniot jump conditions at a certain point in similarity variable space. Once the trajectory multiplier is determined, the Guderley problem is effectively solved.

Despite the preceding and almost entirely mathematical attention devoted to the problem, there is, to the authors' knowledge, no published description of all details required to numerically evaluate its semi-analytic solution. Moreover, there appears to be no example in the literature exploiting the unique features of this challenging problem for the purposes of quantitative code verification of a compressible flow algorithm. Among the contributions of this article, we seek to fill both of these gaps.

The realisation of these goals requires a unified approach to understanding both the mathematical and computational subtleties of the problem. Accordingly, we rigorously examine both the converging and diverging portions of the Guderley solution. We present a reduction of the one-dimensional inviscid flow equations to self-similar form based on Lie Group techniques in the spirit of the work of Coggeshall *et al.* (Coggeshall and Axford 1986, Coggeshall 1991, Coggeshall and Meyer-ter-Vehn 1992), as opposed to ansatz or dimensional arguments.<sup>1</sup> We focus only on the determination of standard solution modes (i.e. not

those implied to exist by Lazarus and Richtmyer (1977) and by Lazarus (1981), and discussed in further detail by Van Dyke and Guttman (1982)).

A complete description of the subtleties involved in the numerical solution of the problem will follow the analytic and semi-analytic considerations; as a corollary to this development, various useful approximations to the value of the similarity exponent – including a new one based on the work of Hirschler and Gretler (2001) – are reconciled in Appendix 1. With all necessary mathematical and computational matters understood, we proceed with what we believe to be the first quantitative verification analysis performed using the Guderley problem. This analysis (reviewed, e.g. by Oberkampf *et al.* (2004) and Roy (2005)) exemplifies the process of determining that a model implementation (e.g. a software instantiation of an algorithm for approximate numerical solution of partial differential equations) accurately represents the developer's conceptual description of and solution to the model. This process complements that of validation analysis, or determining the degree to which a model is an accurate representation of the real world from the perspective of the intended uses of the model (and, thus, necessarily involves the comparison of simulation results with experimental data).

The structure of this article is as follows. In Section 2 we provide a brief review of the Guderley problem. The presentation in Section 3 describes how, using group-theoretic methodology, this problem is reduced to its self-similar form for both the converging-shock and reflected-shock phases. We discuss details surrounding the construction of the semi-analytic ('exact') solution in Section 4. Comparisons of compressible flow code simulations of the Guderley problem with the exact solution are given in Section 5, including quantitative code verification analysis of an Eulerian finite-volume code. We conclude in Section 6.

## 2. Review of the Guderley problem

The 'classical Guderley problem' begins with the consideration of an infinitely strong, symmetric shock wave focusing perfectly on an infinite axis (cylindrical geometry) or point (spherical geometry). The source of the shock wave is not discussed in this scenario, but the initial state of the gas into which the wave is propagating is well-defined. Denoting physical flow variables in this unshocked region by the subscript 0 (see Figure 1), the initial state is given by:

$$u_0(r, t) = 0, \quad (1)$$

$$\rho_0(r, t) = \text{constant}, \quad (2)$$

$$P_0(r, t) = 0, \quad (3)$$

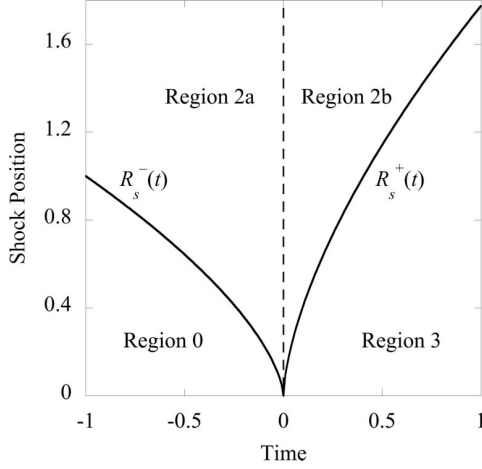


Figure 1. Notional representation of converging shock trajectory  $R_s^-(t)$ , reflected shock trajectory  $R_s^+(t)$ , and space-time regions 0, 2a, 2b, and 3.

where  $r$  denotes position ( $r \geq 0$ ),  $t$  time ( $-\infty < t < 0$  for the converging mode,  $0 < t < \infty$  for the reflected mode),  $u$  velocity,  $\rho$  mass density, and  $P$  material pressure. For a one-dimensional (1-D Cartesian, cylindrical or spherical), smooth flow free of viscosity, heat conduction, radiation and body forces, the Euler equations describe fluid motion at all continuous (i.e. non-shock) locations:

$$\frac{\partial \rho}{\partial t} + \frac{\partial(\rho u)}{\partial r} + (m-1) \frac{\rho u}{r} = 0, \quad (4)$$

$$\frac{\partial u}{\partial t} + u \frac{\partial u}{\partial r} + \frac{1}{\gamma} \left[ \frac{c^2}{\rho} \frac{\partial \rho}{\partial r} + 2c \frac{\partial c}{\partial r} \right] = 0, \quad (5)$$

$$\frac{\partial c}{\partial t} + u \frac{\partial c}{\partial r} + (\gamma-1)c \left[ \frac{\partial u}{\partial r} + \frac{(m-1)u}{r} \right] = 0, \quad (6)$$

where  $c$  denotes the local sound speed, defined through the pressure and density by:

$$c^2 \equiv \gamma P / \rho. \quad (7)$$

Here, we consider only a polytropic gas with the incomplete equation of state (EOS) given by:

$$P(\rho, e) = (\gamma-1)\rho e, \quad (8)$$

where  $e$  is the specific internal energy (SIE). In Equations (4)–(8),  $\gamma$  denotes the adiabatic exponent ( $1 < \gamma < \infty$ ), and  $m$  the space dimension ( $m = 1, 2$ , or  $3$  for 1-D planar, cylindrical or spherical symmetry). Equations (4)–(8) are not valid globally, though shock

jump conditions are available to connect the pre-shock and post-shock flow fields. In particular, since the converging shock wave is assumed to be infinitely strong, the strong limit of the Rankine–Hugoniot jump conditions may be used to connect the flow just upstream to that just downstream:

$$\frac{\rho_{2a}}{\rho_0} = \frac{\gamma+1}{\gamma-1}, \quad (9)$$

$$u_{2a} = \frac{2}{\gamma-1} \dot{R}_s^-(t), \quad (10)$$

$$P_{2a} = \frac{2}{\gamma-1} \rho_0 [\dot{R}_s^-(t)]^2, \quad (11)$$

where the subscript 2a (see Figure 1) denotes the state just downstream of (behind) the converging shock, and  $\dot{R}_s^-(t)$  denotes the converging shock speed.

Equations (9)–(11) are valid for all  $t < 0$  (the convergent mode). After shock focus and subsequent reflection about the axis or point of symmetry (analogous to reflection from a rigid wall in 1-D planar symmetry), these equations cease to be valid. As the strength of the reflected shock wave for  $t > 0$  is unknown (due to the fact that the pressure field upstream (ahead) of the reflected shock wave is once-disturbed and not necessarily negligible), general jump conditions must be employed to connect the flow in the post-reflection space-time regions. After some manipulation, the standard Rankine–Hugoniot jump conditions in this case can be written as (Guderley 1942):

$$\rho_3 = \rho_{2b} \frac{\gamma+1}{\gamma-1 + 2 \left[ c_{2b} / (u_{2b} - \dot{R}_s^+(t)) \right]^2}, \quad (12)$$

$$u_3 = \dot{R}_s^+(t) + \frac{1}{\gamma+1} \left[ u_{2b} - \dot{R}_s^+(t) \right] \times \left\{ \gamma-1 + 2 \left( \frac{c_{2b}}{u_{2b} - \dot{R}_s^+(t)} \right)^2 \right\}, \quad (13)$$

$$P_3 = P_{2b} + \frac{2}{\gamma+1} \rho_{2b} [u_{2b} - \dot{R}_s^+(t)]^2 \times \left\{ 1 - \left( \frac{c_{2b}}{u_{2b} - \dot{R}_s^+(t)} \right)^2 \right\}, \quad (14)$$

where the subscripts 2b and 3 (see Figure 1) denote, respectively, the states just upstream and downstream of the reflected shock, and  $\dot{R}_s^+(t)$  denotes the reflected

shock speed. Additional constraints apply at  $r=0$  for  $t > 0$ :

$$|\rho_3(0, t)| < \infty, \quad (15)$$

$$u_3(0, t) = 0, \quad (16)$$

$$|P_3(0, t)| < \infty. \quad (17)$$

In conjunction with the conditions that the flow field be single-valued for all  $t$  (including  $t=0$  but excepting shock wave positions) and bounded as  $r \rightarrow \infty$  for  $t \neq 0$ , Equations (1)–(17) are sufficient to fully determine the flow field surrounding both the converging and reflected shock waves for all  $t$ .

### 3. Construction of the Guderley solution

Equations (4)–(6) have been found (Axford and Holm 1978, 1981, Ovsiannikov 1982, Axford 2000) to admit the group of point transformations with the generator:

$$\begin{aligned} \hat{U} = & (a_2 + a_3)r \frac{\partial}{\partial r} + (a_1 + a_2)t \frac{\partial}{\partial t} + a_3u \frac{\partial}{\partial u} + a_4P \frac{\partial}{\partial P} \\ & + (a_4 - 2a_3)\rho \frac{\partial}{\partial \rho}, \end{aligned} \quad (18)$$

where the parameters  $a_i$  ( $i=1, 2, 3, 4$ ) are arbitrary constants.

Equations (4)–(6) can be reduced to ordinary differential equations by introducing the invariant functions of the group as the new independent and dependent variables. These functions are determined by solving:

$$\hat{U}\Psi(r, t, u, \rho, P)|_{\Psi=0} = 0, \quad (19)$$

where  $\Psi$  is an arbitrary function of its arguments. Equation (19) is a linear, first order partial differential equation whose solution is found by the method of characteristics. The characteristic equations of Equation (19) are:

$$\frac{dr}{(a_2 + a_3)r} = \frac{dt}{(a_1 + a_2)t} = \frac{du}{a_3u} = \frac{dP}{a_4P} = \frac{d\rho}{(a_4 - 2a_3)\rho}. \quad (20)$$

Invariance of the initial conditions, boundary conditions, etc. (as given in Equations (1)–(3), (9)–(11), (12)–(14) and (15)–(17)) requires the following constraints on the group parameters  $a_i$ ,  $i=1, 2, 3, 4$ :

$$a_4 - 2a_3 = 0, \quad (21)$$

$$a_1 = 0, \quad (22)$$

$$a_2 = 1, \quad (23)$$

$$a_2 + a_3 = \alpha, \quad (24)$$

where  $\alpha$ , the ‘similarity exponent,’ is a dimensionless parameter to be determined in the course of the analysis. Here, Equation (21) expresses the assumption of a uniform ambient medium, Equation (22) reflects that the start time is arbitrary, and Equation (23) indicates that the time variable is not being scaled. With  $a_2 = 1$ , Equation (24) specifies a scaling of the radial coordinate with the similarity exponent  $\alpha$ .

With Equations (21)–(24), (20) becomes

$$\frac{dr}{\alpha r} = \frac{dt}{t} = \frac{du}{(\alpha - 1)u} = \frac{dP}{2(\alpha - 1)P} = \frac{d\rho}{0}, \quad (25)$$

where the zero denominator in the last term reflects the assumption of a uniform ambient medium, as expressed in Equation (21). Solutions of these characteristic equations are:

$$\text{sgn}(t) \frac{r}{k|t|^\alpha} = \text{constant}, \quad (26)$$

$$\frac{u}{r^{1-(1/\alpha)}} = \text{constant}, \quad (27)$$

$$\frac{P}{r^{2-(2/\alpha)}} = \text{constant}, \quad (28)$$

$$\rho = \text{constant}, \quad (29)$$

where  $k$  is an arbitrary dimensional constant that will be set to unity in the numerical calculations. Equations (26)–(29) are the invariant coordinates of the group generator given by Equation (18). If we define:

$$\zeta \equiv \text{sgn}(t) \frac{r}{k|t|^\alpha}, \quad (30)$$

$$v(\zeta) \equiv \frac{u}{r^{1-(1/\alpha)}}, \quad (31)$$

$$p(\zeta) \equiv \frac{P}{r^{2-(2/\alpha)}}, \quad (32)$$

$$d(\zeta) \equiv \rho, \quad (33)$$

then Equations (4)–(6) may be reformulated as ODEs with the new dependent variables  $v$ ,  $p$  and  $d$  as functions of the new independent variable  $\zeta$ . Alternatively, Equations (31)–(33) may be nondimensionalised through the transformations:

$$V(\xi) \equiv v \xi k, \quad (34)$$

$$C(\xi) \equiv \gamma p d(\xi k)^2, \quad (35)$$

$$D(\xi) \equiv \frac{d}{\rho_0}. \quad (36)$$

With Equations (34)–(36) and  $k=1$ , Equations (30)–(33) reduce to:

$$\xi \equiv \operatorname{sgn}(t) \frac{r}{|t|^\alpha}, \quad (37)$$

$$u(r, t) \equiv \frac{r}{t} V(\xi), \quad (38)$$

$$c^2(r, t) \equiv \frac{r^2}{t^2} C(\xi), \quad (39)$$

$$\rho(r, t) \equiv \rho_0 D(\xi). \quad (40)$$

We utilise this non-unique choice of variables and follow the particularly clear development of Chisnell (1998). Lazarus (1981) takes a different approach, using as his fundamental nondimensional independent variable a quantity proportional to  $\xi^{-1/\alpha}$ . This choice of variables has implications in the computational evaluation of the solution, as we discuss in Sections 3.1, 3.2 and 4. A more rigorous and detailed derivation of Equations (37)–(40), including an explanation of the meaning of the group generator given in Equation (18), is provided by Axford and Holm (1978, 1981) and Axford (2000).

Analogs of Equations (4)–(6) may be transformed to a system of ordinary differential equations (ODEs) in the dimensionless variables  $\xi$ ,  $D(\xi)$ ,  $V(\xi)$ , and  $C(\xi)$ :

$$\frac{1}{C} \frac{dC}{dV} = \frac{2\Delta \{1 + \{[(1-\alpha)/\gamma(\alpha-V)]\}\} + (\gamma-1)Q(V)}{\Delta \{mV - [2(1-\alpha)/\gamma]\} + (\alpha-V)Q(V)}, \quad (41)$$

$$\frac{1}{D} \frac{dD}{dV} = \frac{Q(V) - \Delta \{[2(1-\alpha)]/\gamma(\alpha-V)\}}{(\alpha-V)Q(V) + \Delta \{mV - [2(1-\alpha)/\gamma]\}}, \quad (42)$$

$$\frac{1}{\xi} \frac{d\xi}{dV} = \frac{-\Delta}{(\alpha-V)Q(V) + \Delta \{mV - [2(1-\alpha)/\gamma]\}}, \quad (43)$$

where

$$\Delta \equiv -C + (V-\alpha)^2, \quad (44)$$

$$Q(V) \equiv mV(V-\alpha) + \frac{2(1-\alpha)}{\gamma}(\alpha-V) - V(V-1). \quad (45)$$

One can similarly transform Equations (9)–(11), (12)–(14), (15)–(17), and the conditions that the flow field be single-valued for all  $t$  and bounded as  $r \rightarrow \infty$  for  $t \neq 0$ , as these relations are invariant under the same group of point transformations as Equations (4)–(6). Transformation of these expressions results in the following relations. At the incoming shock location:

$$D(\xi = -1) = \frac{\gamma+1}{\gamma-1}, \quad (46)$$

$$V(\xi = -1) = \frac{2\alpha}{\gamma+1}, \quad (47)$$

$$C(\xi = -1) = \frac{2(\gamma-1)\alpha^2}{(\gamma+1)^2}. \quad (48)$$

As  $t \rightarrow 0^-$ :

$$D(\xi \rightarrow -\infty) = \text{constant}, \quad (49)$$

$$V(\xi \rightarrow -\infty) = 0, \quad (50)$$

$$C(\xi \rightarrow -\infty) = 0. \quad (51)$$

At the reflected shock (where  $\xi \equiv \xi_R$ ):

$$D_3(\xi_R) = D_{2b}(\xi_R) \frac{\gamma+1}{\gamma-1 + 2 \left[ C_{2b}(\xi_R)/(V_{2b}(\xi_R) - \alpha)^2 \right]}, \quad (52)$$

$$V_3(\xi_R) = \alpha + \frac{1}{\gamma+1} [V_{2b}(\xi_R) - \alpha] \times \left\{ \gamma-1 + 2 \left[ C_{2b}(\xi_R)/(V_{2b}(\xi_R) - \alpha)^2 \right] \right\}, \quad (53)$$

$$C_3(\xi_R) = \frac{1}{\gamma+1} \left\{ \gamma-1 + 2 \left[ C_{2b}(\xi_R)/(V_{2b}(\xi_R) - \alpha)^2 \right] \right\} \times \left\{ C_{2b}(\xi_R) + \frac{2\gamma}{\gamma+1} [V_{2b}(\xi_R) - \alpha]^2 \right\} \times \left\{ 1 - \left[ \frac{C_{2b}(\xi_R)}{(V_{2b}(\xi_R) - \alpha)^2} \right] \right\}. \quad (54)$$

As  $r \rightarrow 0$  for  $t > 0$ :

$$|D(\xi = 0)| < \infty, \quad (55)$$

$$V(\xi = 0) = \text{constant}, \quad (56)$$

$$C(\xi = 0) \rightarrow \infty. \quad (57)$$

Through the focus:

$$D_{2a}(\xi \rightarrow -\infty) = D_{2b}(\xi \rightarrow \infty), \quad (58)$$

$$\lim_{t \rightarrow 0^+} \frac{r}{t} [V_{2a}(\xi(r, t)) - V_{2b}(\xi(r, t))] = 0, \quad (59)$$

$$\lim_{t \rightarrow 0^+} \frac{r^2}{t^2} [C_{2a}(\xi(r, t)) - C_{2b}(\xi(r, t))] = 0. \quad (60)$$

Together, Equations (41)–(43) and Equations (46)–(60) provide a framework for the Guderley problem in terms of ODEs and additional constraints. Different forms of these governing equations have been previously derived by various authors (Lazarus and Richtmyer 1977, Lazarus 1981, Chisnell 1998).

### 3.1. The converging shock

The calculation of the similarity exponent and evaluation of the numerical solution of Equations (41)–(43) are carried out simultaneously, first using successive estimates for  $\alpha$  and the initial and boundary conditions given by Equations (46)–(48) and Equations (49)–(51). With an initial estimate for  $\alpha$ , numerical integration of Equations (41)–(43) is typically started at the incoming shock represented by Equations (46)–(48) and carried through to the state represented by Equations (49)–(51). Between these states, however, the governing equations become singular when  $\Delta = 0$ . As shown by Chisnell (1998), to remove the physically unrealistic singular behaviour, it becomes necessary to impose the constraint:

$$Q(V^*) = m V^*(V^* - \alpha) + \frac{2(1 - \alpha)}{\gamma} (\alpha - V^*) - V^*(V^* - 1) = 0 \quad \text{when } \Delta = 0, \quad (61)$$

where  $V^*$  represents the  $V$ -coordinate of the  $\Delta = 0$  singularity. Accordingly, the constraint given by Equation (61) provides the means by which to remove this singularity and numerically determine a precise value for the similarity exponent. Concomitantly, the apparent singularity in Equations (41)–(43) becomes integrable, and the numerical solution of these equations may be carried through to the state given by Equations (49)–(51).

In this work, this procedure was implemented using the equations based on the nondimensionalisation of Lazarus (1981).<sup>2</sup> We use the Netlib routines ODE to solve the system of differential equations and the

one-dimensional rootfinder ZEROIN for determining the similarity exponent (Forsythe *et al.* 1977, Netlib 2010).

In the literature (Lazarus and Richtmyer 1977, Lazarus 1981, Hafner 1998, Hirschler and Gretler 2001), there has been inconsistent reproduction of similarity exponent values beyond eight or nine decimal places, even for ‘standard’ values of the adiabatic exponent. For  $\gamma < 1.4$ , accurate calculation of  $\alpha$  becomes difficult, as discussed by Lazarus (1981). The results given in Table 1 are consistent with other published results.

### 3.2. The reflected shock

The converging shock wave solution mode is valid until focus ( $t = 0$ ). At that time, the shock wave reflects about the point or axis of symmetry and proceeds to diverge outwards into the once-perturbed fluid with an unknown trajectory given by:

$$R_s^+(t) = B t^\beta, \quad (62)$$

where the parameters  $B$  and  $\beta$  are initially unknown, though it is easily shown that  $\beta = \alpha$ . The parameter  $B$ , however, requires more effort to calculate.

As the structure of the equations governing the flow for  $t > 0$  has not changed (they are in fact given by Equations (41)–(43)), numerical evaluation of the solution may, with a suitable change of variables (see Lazarus (1981)), be continued beyond the state represented by Equations (49)–(51) by means of two integrations. The first integration represents recovery of flow data beginning at  $r \rightarrow \infty$  for all  $t > 0$ , and can be continued ‘inward’ until the reflected shock wave is reached. Being coupled to the unknown value of  $B$ , the phase-space point corresponding to the reflected shock wave is unknown. If this location were known, then the general-strength Rankine–Hugoniot jump conditions would be applied there, and the integration of Equations (41)–(43) could be continued to a suitable

Table 1. Selected values of the similarity exponent  $\alpha$ .

$\gamma$	Cylindrical geometry ( $m = 2$ )		Spherical geometry ( $m = 3$ )	
	Present work	Lazarus (1981) $1/\lambda_{\text{std}}$	Present work	Lazarus (1981) $1/\lambda_{\text{std}}$
1.4	0.835323192	0.8353231919	0.717174501	0.7171745015
5/3	0.815624901	0.8156249014	0.688376823	0.6883768229
2	0.800112351	0.8001123512	0.667046070	0.6670460703
3	0.775666619	0.7756666194	0.636410594	0.6364105940
6	0.751561684	0.7515616841	0.610339148	0.6103391480

endpoint, namely, until Equations (55)–(57) are satisfied. This final state represents the position  $r = 0$  for  $t > 0$ .

To determine the phase space location of the reflected shock wave, Lazarus (1981) devised a so-called ‘jump locus’ methodology. A locus of ‘jump points’ is formed by applying the general Rankine–Hugoniot jump conditions to every numerical solution point beyond the state represented by Equations (49)–(51), which corresponds to the origin in the  $(V, C)$ -plane. The numerical integration and resulting jump locus are continued to an arbitrary end point in the  $(V, C)$ -plane beyond the phase-space position corresponding to the reflected shock wave. The end point is determined by trial and error, subject to the success of the second numerical integration.

This second numerical integration follows the construction of the jump locus. It is subject to another appropriate change of variables and is initialised from Equations (55)–(57). This integration is continued until a single intersection with the jump locus is obtained. Through this coupling, one identifies a unique phase-space point (on the jump locus) at which the reflected shock wave exists. Through suitable transformations of these results  $B$  is determined, and the entire diverging-phase solution can be constructed. Data from the first numerical integration beyond the location corresponding to the correct jump point are thereby rendered irrelevant; the same is true of the remainder of the jump locus. As for the converging shock calculation, in this work our computational implementation of the reflected shock solution follows the Lazarus methodology.

Lazarus (1981), defining his  $B$  as the reflected shock space–time location, published values of that parameter (found by taking  $B$  in Equation (62) to the negative  $\alpha$  power) in Tables 6.4–6.5 of that reference (subject to the erratum (Lazarus 1982)). As mentioned earlier, for  $\gamma < 1.4$ , accurate calculation of  $B^{-\alpha}$  becomes difficult, as discussed by Lazarus (1981). Even so, the results given in Table 2 are consistent with other published results.

#### 4. Semi-analytic evaluation of the Guderley solution

The overview appearing in Sections 2 and 3 closely follows the traditional developments of Stanyukovich (1970), Meyer-ter-Vehn and Schalk (1982), Chisnell (1998), Zel’dovich and Raizer (2002), Sachdev (2004), and the overwhelming majority of other researchers. As shown in Section 2, however, the self-similar variable system under which the Guderley problem can be analysed is not unique. Evidence exists that some self-similar variable choices are more useful than others for certain applications. For example, the phase

Table 2. Selected values of  $B^{-\alpha}$ , the reflected shock space–time location.

$\gamma$	Cylindrical geometry ( $m=2$ )		Spherical geometry ( $m=3$ )	
	Present work	Lazarus (1981, 1982)	Present work	Lazarus (1981, 1982)
1.4	2.815610935	2.815608	2.688492680	2.688492
5/3	1.694792696	1.694792	1.547894929	1.547896
2	1.199630409	1.199631	1.077253818	1.077255
3	0.763159927	0.763160	0.693969704	0.693970
6	0.540791267	0.5407906	0.531821969	0.5318222

space analysis included in the mathematical analysis of the Guderley problem appears to be most conveniently conducted under the system of variable transformations employed by the aforementioned authors, as summarised in Sections 2 and 3.

A less common – but still viable – self-similar variable system appears in the work of Lazarus (1981). Even as the traditional formulation of the Guderley problem is useful from the standpoint of mathematical analysis, the Lazarus formulation has proven to be computationally advantageous.

Instead of  $\xi$  and  $C$ , this alternative formulation is based on the similarity variables:

$$x \equiv t/r^2, \quad (63)$$

$$c(r, t) \equiv \frac{r}{t} \tilde{C}(x), \quad (64)$$

where, effectively,  $\alpha \equiv 1/\lambda$ , and  $V$  and  $D$  are defined as in Equations (38) and (40), respectively. The phase-space position of the converging shock wave is at  $x = -1$  (where  $t < 0$  again denotes the converging regime), and analogs of Equations (41)–(43) with  $x$  as the independent variable are integrated.

Even though the alternative set of ODEs is still reducible to one governing equation for  $\tilde{C}(V)$  and two supplemental quadratures, we find it advantageous to integrate the system in its  $x$ -dependent form. Foremost, this strategy is preferable computationally because it obviates the necessity of  $\xi \rightarrow -\infty$  through focus: instead,  $x$  passes smoothly through the origin from negative to positive values. Following this passage through focus, the integration continues to the reflected shock phase space location  $x = B^{-\alpha}$ , where analogs of Equations (52)–(54) are applied. The integration then proceeds to  $x \rightarrow \infty$ , which corresponds to  $r \rightarrow 0$  for  $t > 0$ . This state, which represents a singular point of the governing ODEs, will be discussed later.

#### 4.1. Singular analysis

Lazarus (1981) showed that the aforementioned analogs of Equations (41)–(43) contain the variable  $x$  in their denominators, and a number of singular points. While Lazarus identified two of the three relevant singular points, no discussion concerning possible computational problems near them was provided. Following brief descriptions of the singular points, we consider several approaches to avoiding computational difficulties in their vicinities.

The first singular point, denoted  $(V^*, \tilde{C}^*)$  and described in Section 3.1, occurs before focus and involves both the numerators and denominators of each differential equation approaching zero. Near this point, the differential equation for  $\tilde{C}(V)$  has the limiting behaviour:

$$\frac{d\tilde{C}}{dV} = \frac{\tilde{C} - \tilde{C}^*}{V - V^*}, \quad (65)$$

with a solution given by:

$$c_1(\tilde{C} - \tilde{C}^*) = c_2(V - V^*), \quad (66)$$

where  $c_1$  and  $c_2$  are non-zero constants. While the correct values of these constants are determined by analogs of Equations (46)–(48) and the requirement that  $Q=0$  (see Equation (61)), Equation (66) shows that, locally, any straight line through the point  $V = V^*$ ,  $\tilde{C} = \tilde{C}^*$  is a solution.

The second singular point occurs at  $x=0$ , since each of the governing equations contains a factor of  $x$  in the denominator. The third singular point occurs as  $x \rightarrow \infty$ , at which, from Equation (56),  $V$  approaches a constant value. It can be shown that this singularity is a saddle point, but numerical round-off error precludes the semi-analytic solution from staying on the separatrix. As a result,  $V \rightarrow \pm \infty$  in computations, so, in practice, the integration is terminated when  $|V|$  becomes ‘sufficiently large.’ Following this termination, Equation (63) and analogs of Equations (38)–(40) are inverted for the physical flow variables.

There are two approaches to computing the Guderley solution in the vicinity of the singular points. In the first approach, asymptotic expansions of the governing differential equations can be used in the neighbourhood of each singular point.<sup>3</sup> This strategy requires an algorithm for switching between the governing differential equations and asymptotic expansions.

The second approach involves direct integration of the governing ODEs through the singularities and uses no expansions. This case requires a means of assessing loss-of-accuracy in passage through the singularities,

which reveals a second advantage to integrating the governing ODEs in their  $x$ -dependent form. Specifically, the equation for the dimensionless density  $D(x)$  defines the total energy (up to a multiplicative constant) as:

$$E(x) \equiv \frac{\frac{1}{2} D(x) V^2(x) + D(x) C^2(x) / (\gamma(\gamma - 1))}{x^2}. \quad (67)$$

This energy integral is invariant for all  $x$  until the solution trajectory passes through the reflected shock. Consequently, this quantity provides a measure of the solution accuracy near the first two singular points. Thus, the ‘energy check’ is defined as  $\delta E(x) \equiv E(x) - E(x = -1)$ .

We have computed several example solutions of this type using the FORTRAN one-dimensional root-solver algorithm ZEROIN for the determination of  $\alpha$ , and the FORTRAN ODE algorithm for the solution of the governing ODEs (Forsythe *et al.* 1977, Netlib 2010). In these computations, we typically specify the (local) relative error tolerances in these algorithms as  $10^{-15}$  (IEEE double precision). By comparing solution data generated with the ODE algorithm for successive relative error tolerances of  $10^{-j}$ ,  $j=6, \dots, 16$ , the solutions are accurate to approximately 14 digits as the integration begins, and the energy check remains within an order of magnitude of the same figure.

As the numerical integration passes through the first singular point, the energy check is roughly unchanged, which indicates that little accuracy is lost when integrating through the first singular point. In passing through the singular point associated with focus, the energy check decreases to roughly  $10^{-11}$ , suggesting that three to four digits of accuracy are lost in the numerical integration through the second singular point.

These trends appear to hold for all cases of  $m$  and  $\gamma$  appearing in Tables 1 and 2. Since the loss of accuracy in  $\delta E(x)$  is limited to the final three to four digits (out of fourteen), the strategy of integrating through the relevant singular points is sufficiently accurate; as it is simpler than the use of asymptotic expansions, it is a preferable alternative.

#### 4.2. An implementation strategy in compressible flow solvers

The Guderley solution’s infinite extent (i.e. the solution extends to  $r \rightarrow \infty$  for all times) presents a challenge with respect to its use for code verification. We discuss a specific approach to circumvent this challenge in Section 5, but briefly digress here to discuss an alternative strategy.

In this alternate approach, the infinite-extent Guderley solution is used up to a fixed, user-prescribed ‘outer boundary’ far from both the converging and reflected shock waves. At this position, one prescribes a time-dependent boundary condition that is consistent with the Guderley flow occurring within. This boundary condition is simply the time-dependent Guderley solution evaluated at the position of the outer boundary.

In an Eulerian flow solver, the outer boundary location is fixed in space. The flow variable time histories/boundary conditions are obtained from the semi-analytic Guderley solution discussed earlier: the result of the ODE integration is a table of  $D$ ,  $V$  and  $\tilde{C}$  values as functions of  $x$ , between  $x = -1$  and  $x \rightarrow \infty$ . Given the choice of  $r$  corresponding to the outer boundary, and using analogs of the similarity variable definitions Equations (37)–(40), this table is converted to time histories of the physical flow variables at the outer boundary.

A similar prescription for a Lagrangian flow solver is more complicated because the outer boundary, defined by  $r \equiv R(t)$ , is not fixed in space. From Equation (38), however,

$$\frac{dR(t)}{dt} = u(R(t), t) = \frac{R(t)V(x)}{t}. \quad (68)$$

Furthermore, using Equation (63), the phase-space position of the outer boundary  $x_B$  is a function of time only:

$$x_B = \frac{t}{R^\lambda(t)}, \quad (69)$$

a relation that is invertible for  $t = t(x_B)$ . While the function  $R(t)$  is not directly computable, we can construct an ODE that governs the function  $R(x_B)$  using the solution of Equation (69) for  $t = t(x_B)$ . In the following analysis, the subscript  $B$  will be omitted for notational simplicity.

Using the chain rule in conjunction with Equation (68) and multiplying by the quantity  $dt/dx$  yields the equality:

$$\frac{dR}{dt} \frac{dt}{dx} = \frac{dR}{dx} = \frac{R(x)V(x)}{t(x)} \frac{dt(x)}{dx}. \quad (70)$$

Here,  $dt(x)/dx$  is found by implicitly differentiating Equation (69) with respect to  $x$ :

$$\frac{dt(x)}{dx} = \frac{R^\lambda(x)}{1 - \lambda V(x)}, \quad (71)$$

so that, from Equation (70),

$$\frac{dR}{dx} = \frac{R(x)V(x)}{x[1 - \lambda V(x)]}. \quad (72)$$

Solution of Equation (72) is complicated by the inclusion of the dimensionless velocity  $V(x)$ . As a result, Equation (72) must be solved simultaneously with the  $x$ -dependent analogs of Equations (41)–(43). Once this solution is completed, Equation (69) is used to label the resulting table of  $R(x)$  values with corresponding  $t$ -values. The similarity variables  $D$ ,  $V$  and  $\tilde{C}$  are transformed to physical variables as before.

The approach described earlier has been successfully implemented in a Lagrangian compressible flow solver (S. Brandon. Personal communication, 15 June 2007). This method can also be used with an Arbitrary Lagrangian–Eulerian (ALE) solver, if one specifies that the outermost layer of computational cells be in the Lagrangian frame.

## 5. Compressible flow code results

With semi-analytic results for the classical Guderley problem available, a counterpart numerical simulation was conducted using the compressible flow solver of the RAGE code (Gittings *et al.* 2008). This algorithm is a variant of the Lagrange + remap-style Eulerian solver; see (Gittings *et al.* 2008) for further details. With the semi-analytic solution, we can quantitatively gauge the quality of the compressible flow algorithm for both the incoming converging flow as well as the outgoing reflected shock solution.

Initialising a Guderley-like scenario in a generalised compressible flow code must be performed carefully. Theoretically, the converging shock wave that characterises the Guderley problem is created in an infinitely weak state as  $r \rightarrow \infty$  and  $t \rightarrow -\infty$ . The shock wave then propagates inwards with increasing strength due to geometric effects. It is impossible to precisely initialise a compressible flow code with such a prescription. Ponchaut *et al.* (2006) and Hornung *et al.* (2008) initialise generalised Guderley-like compressible flow calculations as ‘spherical shock tubes,’ i.e. by ‘numerically removing a membrane’ separating a small pressure/sound speed differential at some position far from the focal point. The simulation is then allowed to evolve such that a Guderley solution is approached asymptotically in the immediate neighbourhood of the focal point.

To be ostensibly more faithful to the original solution of Guderley (1942), a different approach is employed in this work. Specifically, the solution to the Guderley problem is calculated on a specified, finite domain,  $0 \leq r \leq r_{\max}$ , at a chosen time when the shock

wave is ‘near’ the position  $r=0$ . This computed solution is used to evaluate cell-averaged values on the uniform mesh of the 1D, spherically symmetric compressible flow code. This choice of initialisation is applied over a finite spatial domain including the origin.

In the compressible flow code calculations, a reflecting boundary condition is specified at the far boundary at  $r_{\max}$ , resulting in the generation of a spurious, inward-propagating rarefaction wave. Estimates suggest that this rarefaction wave propagates at approximately the  $u - c$  characteristic speed. This information is used to identify subsets of the computational domains, unpolluted by this spurious rarefaction, on which to make quantitative comparisons of the flow code results with the self-similar Guderley solution computed from the ODEs.

The semi-analytic solution is computed in spherical geometry ( $m=3$ ) for an adiabatic exponent  $\gamma=3$ , reproducing certain results due to Rodríguez and Amable (1978). At  $t=-1$ , the initial state is chosen so that the converging shock is exactly at  $r=1$  (which forms an exact computational-cell boundary in all calculations). With these initial conditions, reflection occurs at the origin at  $t=0$ .

The initial incoming-shock configuration is shown in Figure 2, which depicts the density, velocity, SIE and pressure as functions of radial position over the entire computational domain. In all results and figures,

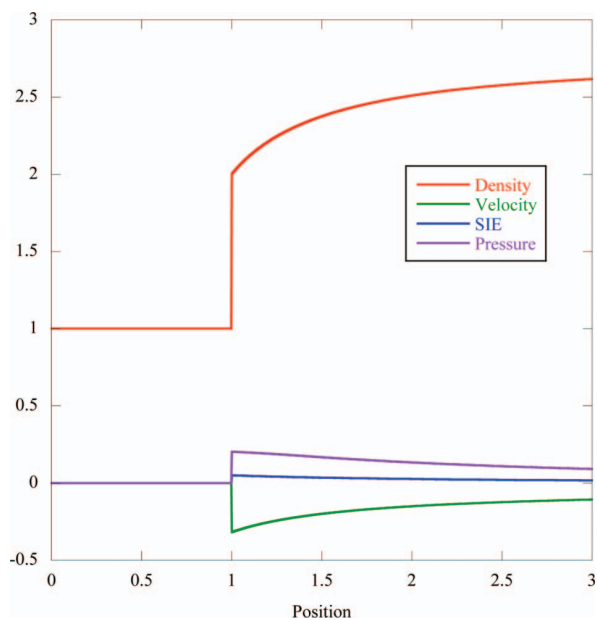


Figure 2. Semi-analytic solution of the Guderley problem for  $\gamma=3$ ,  $m=3$  at initialisation time  $t=-1$ , depicting cell-averaged quantities for 1200 cells between  $r=0$  and  $r=3$ .

flow quantities are in consistent cgs units, commensurate with the default units used in the computed solution.

Without loss of generality, the parameter  $\rho_0$  has been set to unity. The values shown are cell-centred, cell-averaged quantities on 1200 equally-spaced zones between  $r=0$  and  $r_{\max}=3$ . This figure shows that the incoming (negative) velocity peaks at the shock, located at  $r=1$ , as do the pressure and SIE. In the upstream vicinity of the shock, the density gradually decreases to its immediate post-shock value.<sup>4</sup>

The configuration of Figure 2 is used as initial conditions for the compressible flow solver. The semi-analytic and computed density fields at  $t=-0.5$ ,  $-0.1$ ,  $0.1$  and  $0.5$ , are shown in Figures 3–6, respectively. These figures also contain plots of the point-wise error,  $\tilde{y}_j^E - \tilde{y}_j^C$ , in each of the computed solutions; here,  $\tilde{y}_j$  represents the solution averaged over cell  $j$  for either the exact ( $E$ ) or computed ( $C$ ) solution. Corresponding plots of the velocity, SIE, and pressure fields exhibit similar behaviour and are omitted for the sake of brevity. We now turn to a discussion of these results.

### 5.1. Start-up errors

A prominent feature of Figures 3–6 is the ‘dip’ in the computed density fields. This dip is seen to exist in the density solution field for all post-initialisation times. These dips and corresponding bumps in the SIE (not depicted) appear to annihilate one another in the computed pressure field and are not particularly noticeable in velocity results. Quantitative estimates suggest that the dips and bumps move in the fixed Eulerian frame at approximately the material speed.

Phenomena of this type are not unique to the Guderley problem. Dips and bumps such as those observed in Figures 3–6 appear even in simple 1D planar numerical calculations initialised with exact solutions involving shock waves. This phenomenon is discussed in detail by Arora and Roe (1997); see also LeVeque (2002). For the purposes of this investigation, it is sufficient to recognise that density dips appear in systems characterised by nonlinear Hugoniot curves, of which the current case is an example. In such systems, the density dips are an inherent feature of finite volume numerical shock-capturing algorithms. While it is reasonable to assume that details of this phenomenon vary with different compressible flow-algorithms, to the authors’ knowledge there is no evidence in the literature that this phenomenon can be eliminated in Eulerian finite-volume codes.

The magnitude of the start-up error remains approximately constant in time. The spatial extent of the error increases slightly from  $t=-0.5$  to  $t=-0.1$ ,

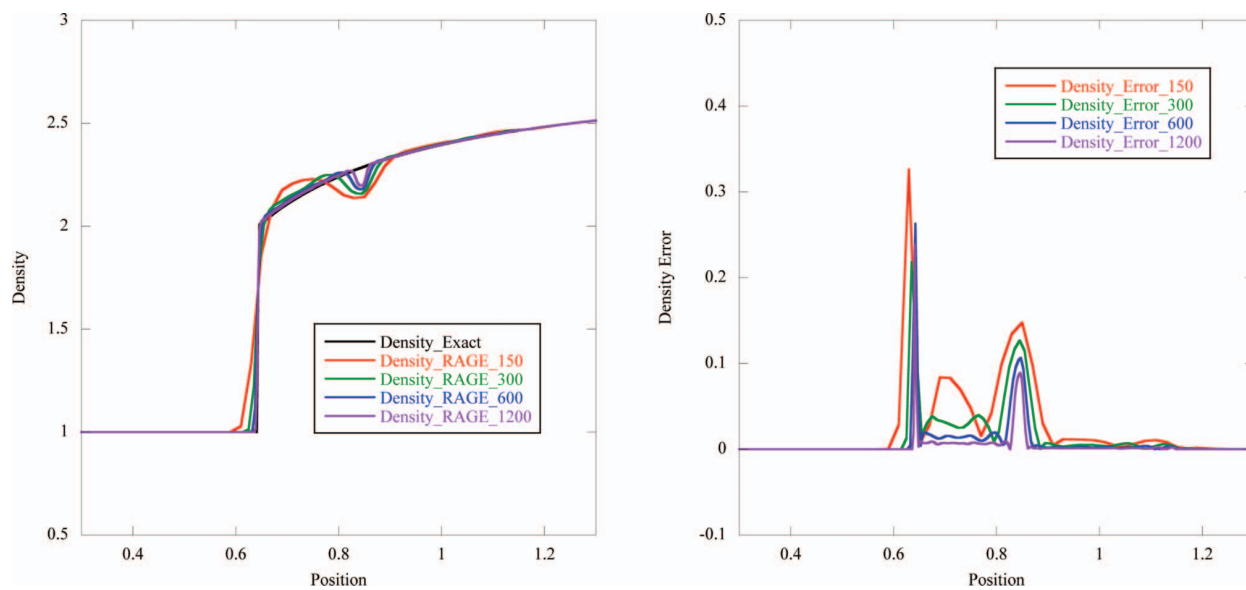


Figure 3. Left: Semi-analytic and computed Guderley density field at  $t = -0.5$ . Right: Corresponding point-wise errors. In these plots, the semi-analytic solution is a black line, and the corresponding computed values are coloured lines according to the legend.

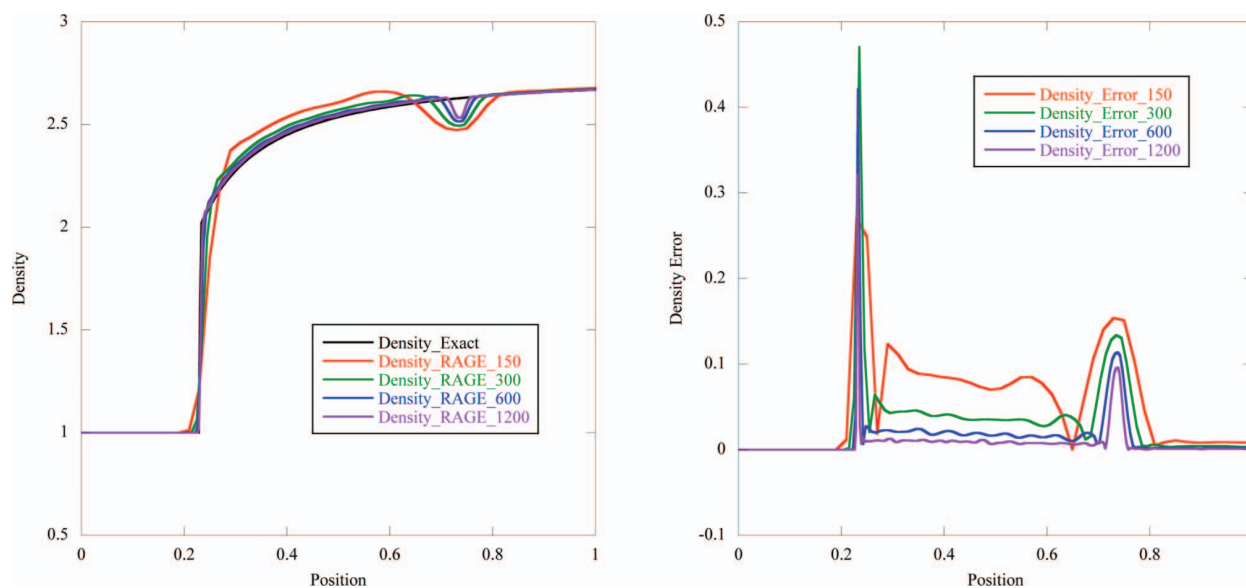


Figure 4. Left: Semi-analytic and computed Guderley density field at  $t = -0.1$ . Right: Corresponding point-wise errors.

but is then compressed at  $t=0.5$ , presumably associated with the passage of the reflected shock. As suggested in Figure 6, however, the presence of the start-up error does little to affect either the position or strength of the reflected shock subsequent to its interaction with this feature.

Figures 5 and 6 suggest that the shock capturing algorithm numerically approximates well the shock focusing and subsequent reflection at the origin at

$t=0$ , i.e. the flow features of the semi-analytic solution subsequent to focus are captured in the computed solution. For only the coarsest resolution does the calculated shock position deviate noticeably from the semi-analytic solution.

For relatively coarse resolutions, Figures 5 and 6 also show evidence of a near-origin error in the density field, similar to the well-known ‘wall heating’ effect seen in the Noh (1987) problem. Figures 5 and 6 also

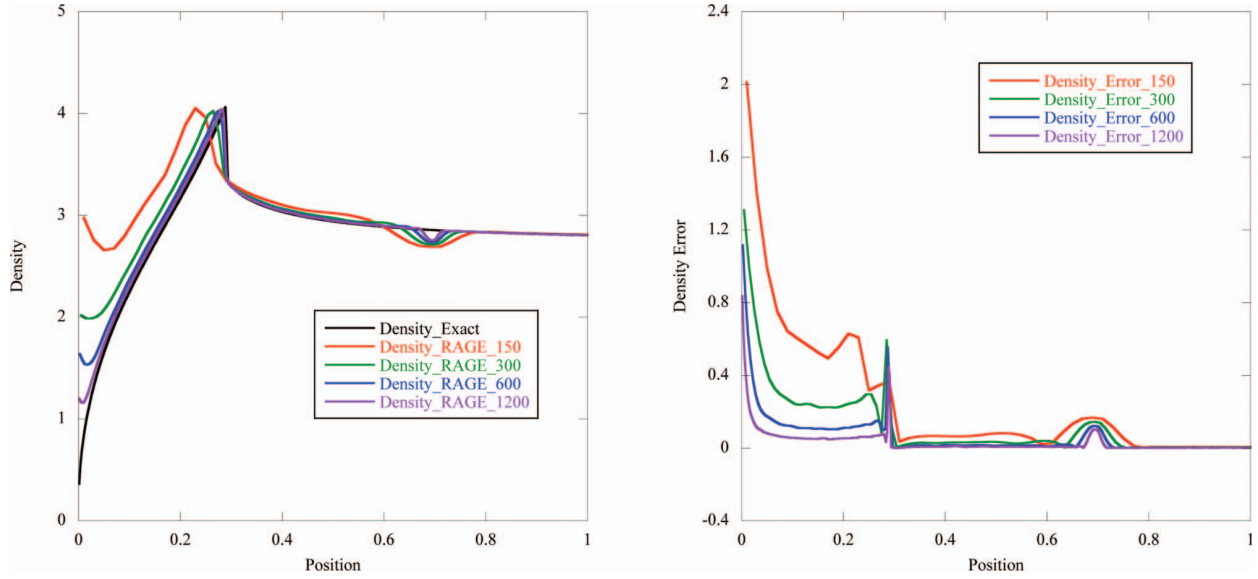


Figure 5. Left: Semi-analytic and computed Guderley density field at  $t=0.1$ . Right: Corresponding point-wise errors.

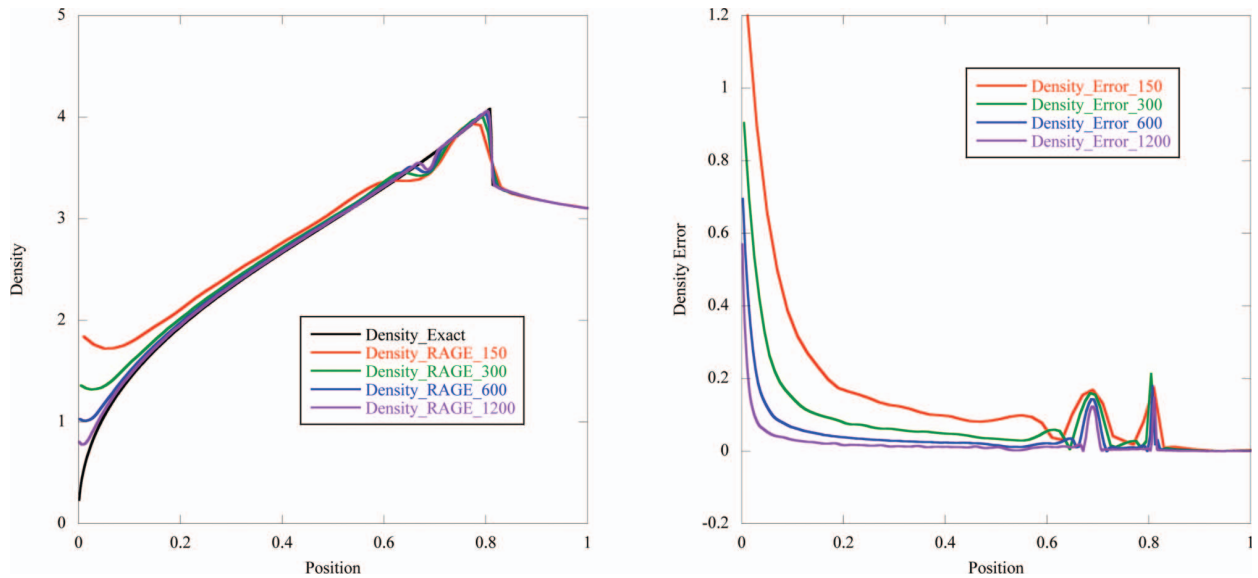


Figure 6. Left: Semi-analytic and computed Guderley density field at  $t=0.5$ . Right: Corresponding point-wise errors.

show that this effect becomes less prominent as the spatial resolution is refined. We expect that the details surrounding this near origin phenomenon are closely related to those thoroughly investigated by Noh (1987), Gehmyer, *et al.* (1997) and Rider (2000) with relevance to the Noh problem.

### 5.2. Effects of initialisation with a post-focus state

The presence of the post-shock errors near the origin led us to question how the compressible flow algorithm

would behave if it were initialised with a post-focus state. Using an initialisation with a state subsequent to shock focusing time, we find the computed behaviour to be more precise than with the converging flow initialisation. Specifically, we evaluate the semi-analytic solution at a time ( $t=0.018594543$  for  $m=3$  and  $\gamma=3$ ) when the shock is located at  $r=0.1$ , and use those values to initialise the compressible flow code. Figure 7 depicts the density, velocity, SIE and pressure as functions of radial position over a subset of the computational domain. These values are cell-centred,

cell-averaged quantities on 1200 equally-spaced zones between  $r=0$  and  $r=3$ . This figure shows the strong peaks in pressure, velocity and density behind the outgoing shock as it encounters the incoming flow.

Comparison between the computed results at  $t=0.5$  in Figures 6 and 8 corresponding to the different initialisations reveals two significant differences. The

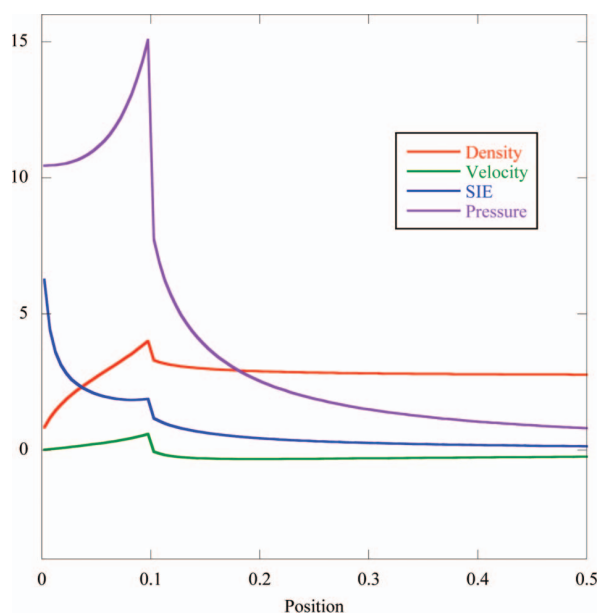


Figure 7. Semi-analytic solution of the Guderley problem at initialisation time  $t=0.018594543$ , depicting cell-averaged quantities for 1200 cells between  $r=0$  and  $r=3$ .

first difference is the near-origin behaviour. Clearly, a choice of post-reflection initialisation drastically reduces the near-origin error – a fact explained by the computed solution not being subject to the consequences of singular behaviour at  $t=0$ .

The second difference is the significant reduction (but not elimination) of the density start-up error in Figure 8: a small, localised flow error is apparent in this figure between  $r=0.1$  and  $r=0.15$ . We speculate that this feature has the same cause as the start-up error evident in Figures 4–6. A possible explanation as to why this phenomenon has smaller amplitude and spatial extent is given by the different flow geometry of the two different initial conditions: the initialisation at  $t=-1$  corresponds to converging flow, while an initialisation with a semi-analytic solution at any  $t > 0$  (including that shown in Figure 7) corresponds to diverging flow. We hypothesise that the divergent flow reduces the start-up errors.

### 5.3. Verification analysis

Code verification analysis is an approach for gathering quantitative evidence that software for the solution of discretized equations generates results consistent with the corresponding continuum equations, e.g. by examining the error order-of-accuracy of the numerical results. Verification analysis (reviewed, e.g. by Oberkampf *et al.* (2004) and Roy (2005)) is a vitally important aspect of both algorithm and software development. The Guderley problem presents an ideal configuration with which to perform code verification

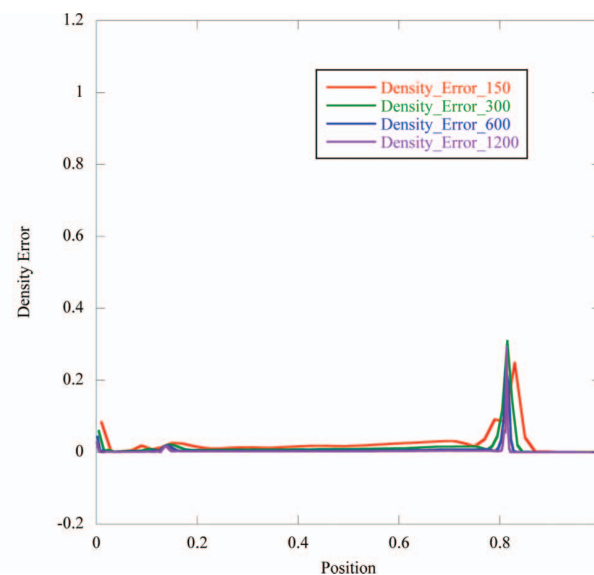
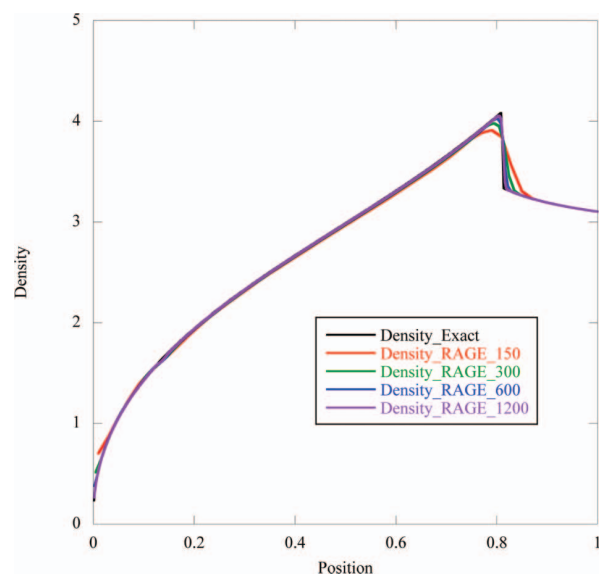


Figure 8. Left: Semi-analytic and computed Guderley density field at  $t=0.5$ , computed from the initial conditions in Right: Corresponding point-wise errors.

analysis for cylindrically or spherically symmetric, converging-then-diverging compressible flow of an ideal gas. Using both the semi-analytic ('exact') and numerical ('computed') Guderley solutions, we evaluate the spatial convergence properties of the RAGE compressible flow algorithm.

Table 3. Summary of  $L_1$ -norm convergence data.

$t$	Premultipliers $A$			
	$\rho$	$u$	$P$	$e$
-0.5	0.1886	0.1003	0.0510	0.0146
-0.1	0.2636	0.0364	0.0593	0.0178
+0.1	0.3078	0.0630	0.2102	0.0278
+0.5	0.2584	0.0547	0.1024	0.0275
+0.5*	0.1780	0.0460	0.1243	0.0091

Note: \*Initialised at  $t = +0.018594543$ ; others initialised at  $t = -1$ .

Table 4. Summary of  $L_1$ -norm convergence data.

$t$	Convergence rates $\sigma$			
	$\rho$	$u$	$P$	$e$
-0.5	0.8652	1.046	1.028	0.9906
-0.1	0.9061	0.9720	1.002	0.9518
+0.1	0.9125	0.9794	0.9358	0.9324
+0.5	0.8501	0.9362	0.8694	0.9401
+0.5*	0.9605	1.011	0.9695	0.9444

Note: \*Initialised at  $t = +0.018594543$ ; others initialised at  $t = -1$ .

We take as axiomatic the standard error ansatz,

$$\|y^E - y^C\| = A (\Delta r)^\sigma, \quad (73)$$

where the superscripts  $E$  and  $C$  refer to the exact and computed solutions,  $\|\cdot\|$  represents an error norm evaluated over a specified domain,  $\Delta r$  is a characteristic mesh dimension (e.g. the cell size on a uniform grid),  $A$  is a prefactor, and  $\sigma$  is the convergence rate (e.g.  $\sigma = 1$  for a first-order method). As is standard for analysis of compressible flows, we consider the  $L_1$  norm only (see, e.g. the monograph of Bouchut (2004)). We approximate the left side of Equation (73) as:

$$\|y^E - y^C\| \approx \frac{1}{\mathcal{V}} \sum_{j=1}^{N_r} |\tilde{y}_j^E - \tilde{y}_j^C| d\mathcal{V}_j, \quad (74)$$

where  $\tilde{y}_j$  represents the solution averaged over cell  $j$  for either the exact ( $E$ ) or computed ( $C$ ) solution,  $d\mathcal{V}_j$  is the volume of the spherical shell element centred at  $r_j$ ,  $N_r$  is the number of cells between the origin and  $r = 2$ , and  $\mathcal{V}$  is the volume of the sphere of radius 2.

The ansatz in Equation (73) assumes that the convergence is monotonic and the method is consistent, i.e. that there is no  $O(1)$  error. Using a series of calculations at different mesh resolutions, it is straightforward to infer best-fit values for both  $A$  and  $\sigma$ , which we accomplish with a standard nonlinear least-squares technique, using software described by Hemez *et al.* (2006). In all calculations, the domain over which the errors were evaluated was  $0 < r < 2$ ,

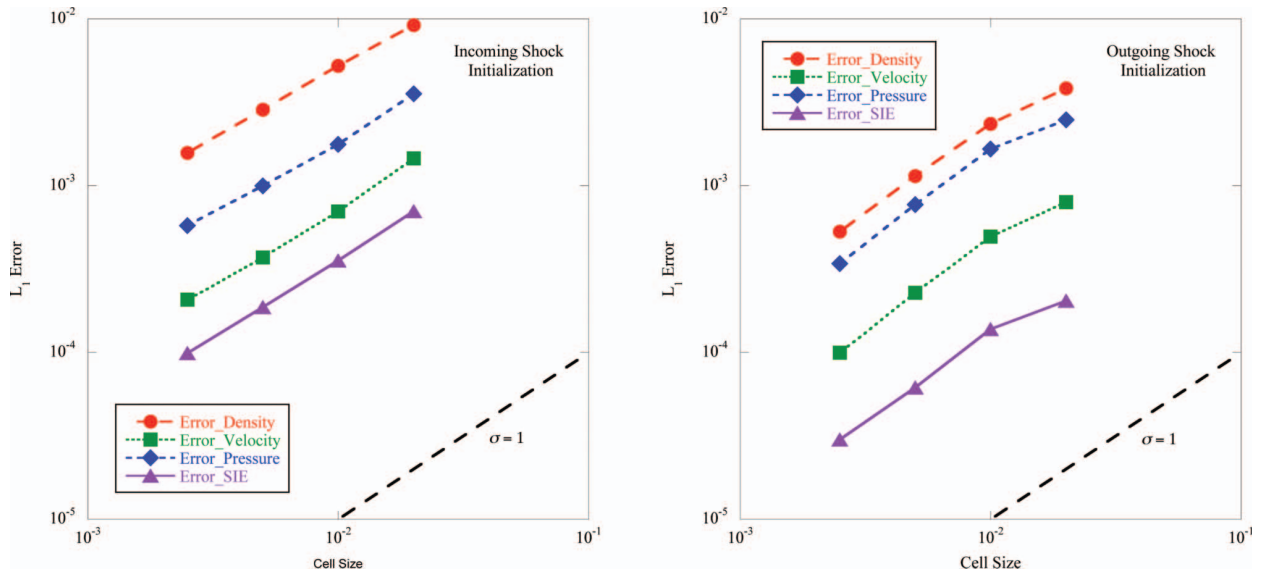


Figure 9.  $L_1$  errors on  $0 \leq r \leq 2$  for flow quantities calculated for the Guderley problem at time  $t = 0.5$ . Left: Problem initiated with incoming shock wave. Right: Problem initiated with outgoing shock wave. The dashed black line in each plot is a reference line for first-order convergence.

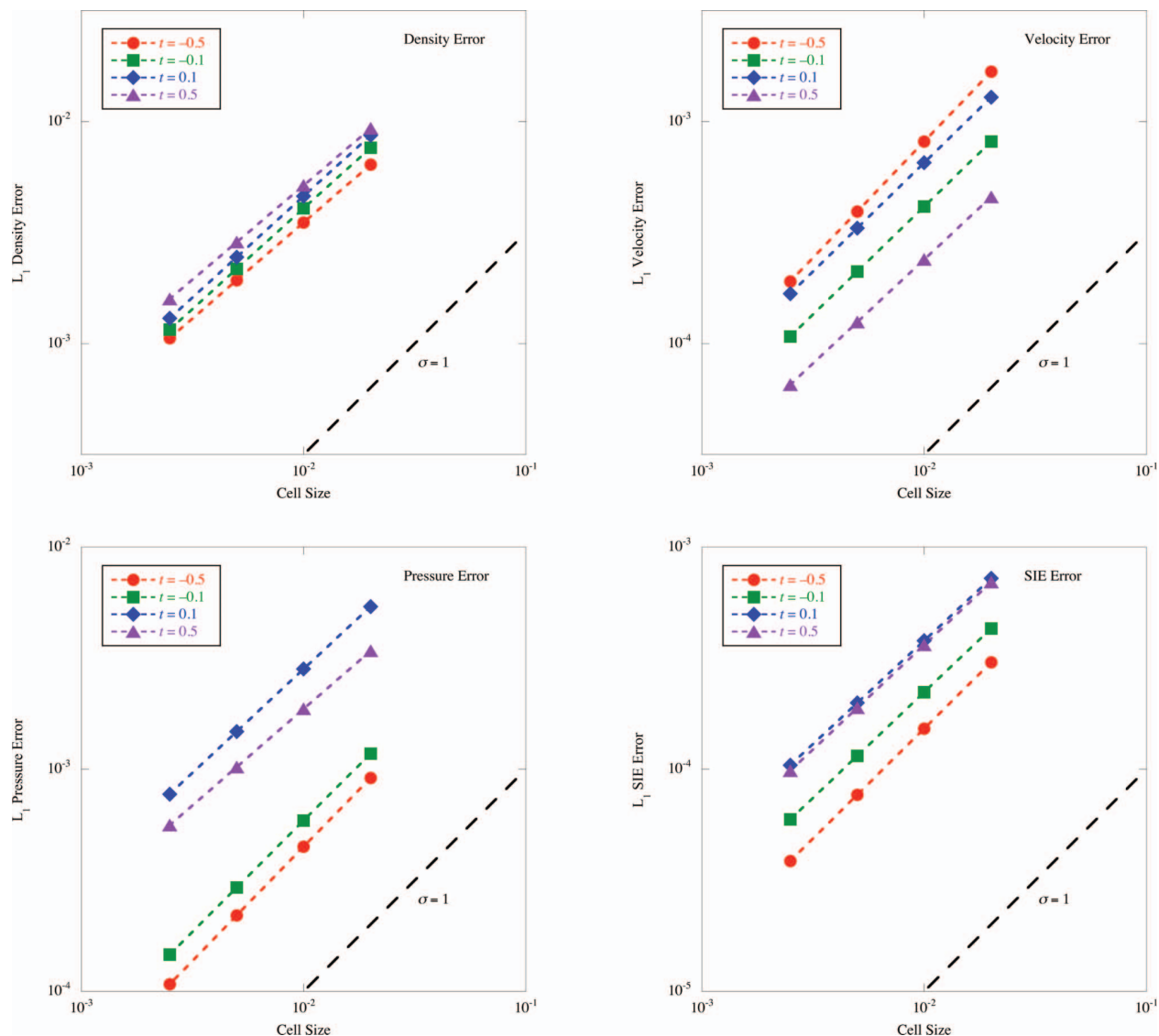


Figure 10.  $L_1$  errors on  $0 \leq r \leq 2$  for flow quantities calculated for the Guderley problem at times  $t = -0.5, -0.1, 0.1, 0.5$ , for initialisation at  $t = -1.0$ . Top left: Density errors. Top right: Velocity errors. Bottom left: Pressure errors. Bottom right: SIE errors. The dashed black line in each plot is a reference line for first-order convergence.

thus neutralising the effects of spurious boundary-driven rarefaction waves, as discussed in Section 5.1.

Results of this analysis are catalogued for various times in Tables 3 and 4. In addition, example plots corresponding to the two data sets given at  $t = 0.5$  (converging and diverging initialisation) are provided in Figure 9. Results for convergent initialisation are provided in the first four rows of the tables and the left plot in this figure; the last row and right plot show results for divergent initialisation.

These results show that the  $L_1$ -norm convergence is approximately linear for times before focus, with the exception of the density field. For times following focus, the  $L_1$ -norm convergence is universally but only

slightly sublinear. In all fields except density, the  $L_1$ -norm convergence rate also decreases as focus is approached. In addition, for times after focus, the  $L_1$ -norm convergence rates decrease for all fields except SIE. The pressure and SIE convergence rates decrease through focus. These trends are further illuminated in Figure 10, which contains plots of the error vs. cell size for these physical variables, at four selected simulation times: two before focus ( $t = -0.5, -0.1$ ) and two after ( $t = 0.1, 0.5$ ). While all errors decrease with increasing mesh resolution (i.e. smaller cell size), only for the density are these monotonic in time; the other quantities exhibit non-monotonic error behaviour. This phenomenon is due to numerical loss-

of-precision in both the exact and computed solutions near the  $t=0$  focus time, as discussed at length in Section 4.

Comparison of the error plots in Figure 9 confirms what is seen for the density in Figures 6 and 8, namely, the absolute error is smaller for the reflected shock initialisation; moreover, the convergence rate in this case is higher. We observe similar trends for each flow quantity except the SIE.

The behaviour observed in Tables 3 and 4, and in Figure 9, illuminates several prominent trends that influence various observed convergence rates:

- (1) Decreases in convergence rates during the time-evolution of the convergent solution mode.
- (2) Decreases in convergence rates during the time-evolution of the diverging solution mode.
- (3) Decreases in convergence rates across focusing time.
- (4) The inapplicability of trends 1 and 3 to the density field.
- (5) A marked improvement in convergence rates for initialisation at a post-focus time.

Trends 1, 2 and 3 have a common explanation. At focus time, the exact Guderley solution for the physical velocity, SIE and pressure fields increases without bound at the shock. This phenomenon is not computationally realisable due to inherent numerical precision limitations, so errors accrue in both the semi-analytic solution and compressible flow code results near focus time. Trends 1 and 3 do not apply to the density field convergence rates, and, in fact, these rates exhibit opposite behaviour. A phenomenon that is responsible for this counterintuitive behaviour is the interaction between a prominent start-up error and the fact that the density field solution does not increase without bound in the vicinity of  $t=0$ . Similar reasoning explains behaviour in the pressure field that does not agree with trends 1–4, as this variable is connected to the density and SIE through the polytropic EOS. Trend 5 notes an improvement in all  $L_1$ -norm convergence rates for a positive choice of initialisation time, in all cases reaching essentially linear levels. This effect is clearly due to improved near-origin behaviour and start-up error reduction in this case.

## 6. Conclusion

We have provided an overview of the theoretical framework necessary to construct a semi-analytic solution to Guderley’s imploding shock problem. This overview contained results based upon the systematic theory of continuous point transformations, as opposed to more common ansatz or dimensional analysis arguments.

Following the theoretical developments, we provided a description of computational procedures used to generate a semi-analytic (exact) solution. This discussion included a detailed description of the numerical procedures employed to ensure solution accuracy when integrating through the singular points in the solution.

We used the semi-analytic solution to the Guderley problem to initialise a compressible flow code on a finite domain and conduct what appears to be the first rigorous code verification analysis of an Eulerian compressible flow solver on this problem. Despite the well-known start-up errors that the computed solutions exhibit, these results show near-linear spatial convergence in the  $L_1$ -norm for the converging solution mode; when this solution is continued through the reflection at the origin, entirely sublinear spatial convergence in the  $L_1$ -norm for the subsequent diverging solution mode. When initialised with a post-focus flow state, the errors in the computed solutions are notably smaller and the convergence results are marginally better.

The Guderley problem provides an attractive and challenging alternative to two other widely-used compressible flow test problems: the Noh problem (Noh 1987, Axford 2000) and the Sedov (1959) problem. The Guderley problem’s advantages lie in the fact that it is capable of describing coupled converging and diverging flow. It will be of interest to use the Guderley problem to evaluate the properties of other compressible flow algorithms, as well as to investigate 2D and 3D geometries. Despite being introduced almost 70 years ago, the Guderley problem continues to challenge the theoretical and computational fluid physics communities, providing an excellent opportunity for code verification analyses.

## Acknowledgements

This work was performed under the auspices of the United States Department of Energy by Los Alamos National Security, LLC, at Los Alamos National Laboratory under contract DE-AC52-06NA25396, and at Sandia National Laboratories, a multi-programme laboratory operated by Sandia Corporation, a wholly owned subsidiary of Lockheed Martin company, for the US Department of Energy’s National Nuclear Security Administration under contract DE-AC04-94AL85000. SDR and JRK acknowledge the support of the US Department of Energy Advanced Strategic Computing Program Verification Project under project leaders J. Brock and F. Hemez. The authors thank M. Clover, J. Grove, G. Hutchens, W. Rider and T. Trucano for valuable insights on these topics, and acknowledge the helpful comments of the anonymous reviewers.

## Notes

1. Dimensional analysis finds *only* scale-invariant variables and solutions, while application of Lie group techniques systematically identifies *all* invariant functions and solutions.
2. In Section 4, we present the reasons for utilising the Lazarus methodology in the numerical calculations

together with computational details useful for practical implementations.

3. Some of the developments appearing in Appendix 1 make use of this methodology, but for a different purpose.
4. Cell averages are determined from numerical integrations using conserved quantities. See Appendix 2 for a discussion.
5. These approximations are to be contrasted with the purely curve-fit approximation for  $\alpha$  as a function of  $\gamma$  given by Hafner (1982) for the spherical ( $m=3$ ) case:

$$\alpha = \{[(\gamma - 1)/(2a)] + (1 - \alpha_\infty)^{-n}\}^{-1/n} + \alpha_\infty, \quad (\text{A1})$$

where  $a = 3.26 \times 10^{-4}$ ,  $n = 6$ , and  $\alpha_\infty = 0.375$ .

6. Timmes *et al.* (2009) provide a detailed discussion of this issue for another compressible flow problem.

## References

- Arora, M. and Roe, P., 1997. On postshock oscillations due to shock capturing schemes in unsteady flows. *Journal of Computational Physics*, 130, 25–40.
- Atzeni, S. and Meyer-ter-Vehn, J., 2004. *The physics of inertial fusion*. New York: Oxford University Press.
- Axford, R., 2000. Solutions of the Noh problem for various equations of state using lie groups. *Lasers and Particle Beams*, 18, 93–100.
- Axford, R. and Holm, D., 1978. Spherical shock collapse in a non-ideal medium. In: *Proceedings of the joint IUTAM/IMU symposium, group theoretical methods in mechanics*, 25–28 August, Novosibirsk, USSR. IUTAM, 47–56.
- Axford, R. and Holm, D., 1981. Converging finite-strength shocks. *Physica D*, 2, 194–202.
- Bilbao, L. and Gratton, J., 1996. Spherical and cylindrical convergent shocks. *Nuovo Cimento*, 18, 1041–1060.
- Bouchut, F., 2004. *Nonlinear stability of finite volume methods for hyperbolic conservation laws and well-balanced schemes for sources*. Basel, Switzerland: Birkhäuser Verlag.
- Brushlinskii, K., 1982. Instability of a convergent spherical shock wave. *USSR Computational Mathematics and Mathematical Physics*, 22, 193–205.
- Butler, D., 1954. *Converging spherical and cylindrical shocks*. Technical report 54/54, UK Armament Research Establishment.
- Chester, W., 1954. The quasi-cylindrical shock tube. *Philosophical Magazine*, 45, 1293–1301.
- Chisnell, R., 1957. The motion of a shock wave in a channel, with applications to cylindrical and spherical shock waves. *Journal of Fluid Mechanics*, 2, 286–298.
- Chisnell, R., 1998. An analytic description of converging shock waves. *Journal of Fluid Mechanics*, 354, 357–375.
- Clarisse, J.M., 2007. *A Godunov-type method in Lagrangian coordinates for computing linearly-perturbed spherically-symmetric flows of gas dynamics* [online]. Available from: <http://hal.archives-ouvertes.fr/hal-00197498> [Accessed 15 December 2011].
- Clark, D. and Tabak, M., 2006. *Isochoric implosions for fast ignition*. Technical report UCRL-CONF-221925, Lawrence Livermore National Laboratory.
- Coggeshall, S., 1991. Analytic solutions of hydrodynamics equations. *Physics of Fluids A*, 3, 757–769.
- Coggeshall, S. and Axford, R., 1986. Lie group invariance properties of radiation hydrodynamics equations and their associated similarity solutions. *Physics of Fluids*, 29, 2398–2420.
- Coggeshall, S. and Meyer-ter-Vehn, J., 1992. Group-invariant solutions and optimal systems for multidimensional hydrodynamics. *Journal of Mathematical Physics*, 33, 3585–3601.
- Fernández, M., 1977. *Implosiones y explosiones en medios condensados*. Thesis (PhD). Escuela Técnica Superior de Ingenieros Aeronáuticos, Madrid.
- Fink, M., Hillebrandt, W., and Röpke, F., 2007. Double-detonation supernovae of sub-Chandrasekhar mass white dwarfs. *Astronomy & Astrophysics*, 476, 1133–1143.
- Forsythe, G., Malcolm, M., and Moler, C., 1977. *Computer methods for mathematical computations*. Englewood Cliffs, NJ: Prentice-Hall.
- Gehmyer, M., Cheng, B., and Mihalas, D., 1997. Nohs constant-velocity shock problem revisited. *Shock Waves*, 7, 255–274.
- Gittings, M., *et al.*, 2008. The RAGE radiation-hydrodynamics code. *Computational Science & Discovery*, 1, 015005–015005.
- Guderley, G., 1942. Starke kugelige und zylindrische Verdichtungsstöße in der Nähe des Kugelmittelpunktes bzw. der Zylinderachse. *Luftfahrtforschung*, 19, 302–312.
- Gurovich, V. and Fel, L., 2009. Landau-Stanyukovich rule and the similarity parameter for converging shocks. *JETP Letters*, 89, 14–18.
- Häfele, W., 1956. Über die Stabilität des Guderleyschen kugeligen Verdichtungsstoßes. *Z. Naturforschung*, 11, 183–186.
- Hafner, P., 1982. *Verdichtung und Reaktivitätsaufbau bei der Zündung von Kernspaltungswaffen, Teil 1: analytische Näherung zum einfallenden Guderleyschen Verdichtungsstoß*. Technical report 109, Fraunhofer-Institut für Naturwissenschaftlich-Technische Trendanalysen (INT).
- Hafner, P., 1998. Strong convergent shock waves near the center of convergence: a power series solution. *SIAM Journal of Applied Mathematics*, 48, 1244–1261.
- Hemez, F., Brock, J., and Kamm, J., 2006. Non-linear error ansatz models in space and time for solution verification. In: *Proceedings of the 47th AIAA/ASME/ASCE/AHS/ASC Structures, Structural Dynamics, and Materials (SDM) Conference and 8th Non-Deterministic Approaches (NDA) Conference*, 1–4 May, Newport, RI, USA. New York: AIAA Press.
- Hirschler, T., 2002. A parametric study of self-similar collapsing shock waves in radiating gas. *Physics of Fluids*, 14, 1491–1501.
- Hirschler, T. and Gretler, W., 2001. On the eigenvalue problem of imploding shock waves. *Zeitschrift für angewandte Mathematik und Physik*, 52, 151–166.
- Hornung, H., Pullin, D., and Ponchaut, N., 2008. On the question of universality of imploding shock waves. *Acta Mechanica*, 201, 31–35.
- Jena, J. and Sharma, V., 1999. Self-similar shocks in a dusty gas. *International Journal of Non-Linear Mechanics*, 34, 313–327.
- Lazarus, R., 1980. Comments on “analysis of spherical imploding shocks”. *Physics of Fluids*, 23, 844–844.
- Lazarus, R., 1981. Self-similar solutions for converging shocks and collapsing cavities. *SIAM Journal of Numerical Analysis*, 18, 316–371.
- Lazarus, R., 1982. Erratum: self-similar solutions for converging shocks and collapsing cavities. *SIAM Journal of Numerical Analysis*, 19, 1090–1090.
- Lazarus, R. and Richtmyer, R., 1977. *Similarity solutions for converging shocks*. Technical report LA-6823-MS, Los Alamos Scientific Laboratory.

- LeVeque, R., 2002. *Finite volume methods for hyperbolic problems*. Cambridge, UK: Cambridge University Press.
- Madhumita, G. and Sharma, V., 2003. Propagation of strong converging shock waves in a gas of variable density. *Journal of Engineering Mechanics*, 46, 55–68.
- Meyer-ter-Vehn, J. and Schalk, C., 1982. Selfsimilar spherical compression waves in gas dynamics. *Zeitschrift für Naturforschung A*, 37, 955–969.
- Mishkin, E., 1980. Reply to comments by Roger B. Lazarus. *Physics of Fluids*, 23, 844–846.
- Mishkin, E. and Fujimoto, Y., 1978a. Analysis of a cylindrical imploding shock wave. *Journal of Fluid Mechanics*, 89, 61–78.
- Mishkin, E. and Fujimoto, Y., 1978b. Analysis of spherically imploding shocks. *Physics of Fluids*, 21, 1933–1938.
- Morawetz, C., 1951. *Contracting spherical shocks treated by a perturbation method*. Thesis (PhD). New York University.
- Motz, H., 1979. *The physics of laser fusion*. New York: Academic Press.
- Netlib., 2010. *Netlib repository at UTK and ORNL*. [online]. Available from: <http://www.netlib.org/> [Accessed 15 December 2011].
- NiCastro, J., 1970. Similarity analysis of the radiative gas dynamic equations with spherical symmetry. *Physics of Fluids*, 13, 2000–2006.
- Noh, W., 1987. Errors for calculations of strong shocks using an artificial viscosity and an artificial heat flux. *Journal of Computational Physics*, 72, 78–120.
- Oberkampf, W., Trucano, T., and Hirsch, C., 2004. Verification, validation, and predictive capability in computational engineering and physics. *Applied Mechanics Reviews*, 57, 345–384.
- Ovsianikov, L., 1982. *Group analysis of differential equations*. New York: Academic Press.
- Ponchaut, N., 2005. *Part I: 3DPTV: advances and error analysis. Part II: extension of Guderley's solution for converging shock waves*. Thesis (PhD). California Institute of Technology.
- Ponchaut, N., et al., 2006. On imploding cylindrical and spherical shock waves in a perfect gas. *Journal of Fluid Mechanics*, 560, 103–122.
- Rider, W., 2000. Revisiting wall heating. *Journal of Computational Physics*, 162, 395–410.
- Rodríguez, M. and Amable, L., 1978. Implosiones auto-semejantes isentropicas y no isentropicas. Technical report J.E.N. 405, Junta de Energía Nuclear.
- Roy, C., 2005. Review of code and solution verification procedures for computational simulation. *Journal of Computational Physics*, 205, 131–156.
- Rygg, J., 2006. *Shock convergence and mix dynamics in inertial confinement fusion*. Thesis (PhD). Massachusetts Institute of Technology.
- Sachdev, P., 2004. *Shock waves and explosions*. Boca Raton, FL: Chapman and Hall/CRC Monographs.
- Sedov, L., 1959. *Similarity and dimensional methods in mechanics*. New York: Academic Press.
- Stanyukovich, K., 1970. *Unsteady motion of continuous media*. New York: Pergamon Press.
- Timmes, F., et al., 2009. *On a cell-averaged solution to the Coggshall #8 problem*. Technical report LA-UR-09-04438, Los Alamos National Laboratory.
- Toqué, N., 2001. Self-similar implosion of a continuous stratified medium. *Shock Waves*, 11, 157–165.
- Van Dyke, M. and Guttman, A., 1982. The converging shock wave from a spherical or cylindrical piston. *Journal of Fluid Mechanics*, 120, 451–462.
- Wang, J., 1982. On the theory of imploding shocks. *Journal of Applied Mathematics and Physics*, 33, 53–62.
- Whitham, G., 1958. On the propagation of shock waves through regions of non-uniform area or flow. *Journal of Fluid Mechanics*, 4, 337–360.
- Wu, C. and Roberts, P., 1996. Structure and stability of a spherical shock wave in a Van der Waals gas. *Quarterly Journal of Mechanics and Applied Mathematics*, 49, 501–543.
- Yousaf, M., 1986. Imploding spherical and cylindrical shocks. *Physics of Fluids*, 29, 680–684.
- Zel'dovich, Y. and Raizer, Y., 2002. *Physics of shock waves and high-temperature hydrodynamic phenomena*. Mineola, NY: Dover Publications.

### Appendix 1. Analytic similarity exponent estimates

The nonlinear eigenvalue problem whose solution determines  $\alpha$  has been solved approximately by a number of authors including Stanyukovich (1970) and Chisnell (1998). There exist a variety of physical and mathematical arguments that provide accurate estimates of the parameter  $\alpha$ . We consider three approximations of  $\alpha$  based on fundamental assumptions about the solution of the governing equations.<sup>5</sup>

$$\alpha = \{[(\gamma - 1)/(2a)] + (1 - \alpha_\infty)^{-n}\}^{-1/n} + \alpha_\infty, \quad (\text{A1})$$

where  $a = 3.26 \times 10^{-4}$ ,  $n = 6$ , and  $\alpha_\infty = 0.375$ .

These estimates ultimately prove useful as first iterates or bracketing values on the true value of  $\alpha$  (see Figure A1), and are easily incorporated into numerical routines that converge to the true value of the similarity exponent. It will be shown that for different ranges of  $\gamma$  and  $m$ , the relative accuracies of the approximations vary.

#### A.1.1. The pressure maximum requirement

Stanyukovich (1970) noted that for certain values of the adiabatic exponent, the pressure distribution behind the converging shock wave contains a single maximum.

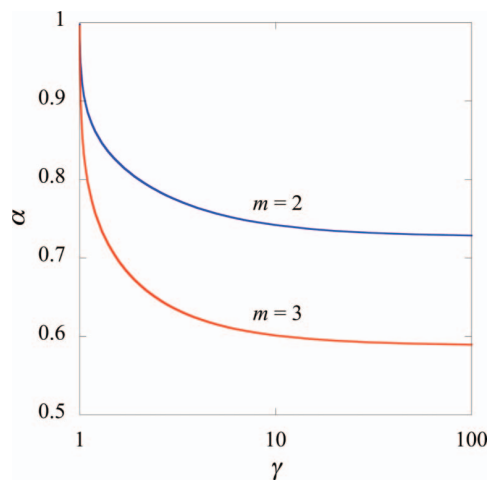


Figure A1. Exact values (Lazarus 1981) of the similarity exponent  $\alpha$  plotted as a function of the polytropic index  $\gamma$  for cylindrical ( $m = 2$ ) and spherical ( $m = 3$ ) geometries.

The existence of a pressure maximum in the flow behind a converging shock wave for arbitrary  $\gamma > 1$  was dismissed by Zel'dovich and Raizer (2002), but a work by Mishkin and Fujimoto (M&F) claimed otherwise (Mishkin and Fujimoto 1978a,b). Through this requirement, M&F derived an analytic expression for  $\alpha$  claimed to be exact:

$$\alpha = \frac{\gamma + 2 + 2\sqrt{2\gamma}}{m\gamma + 2 + 2\sqrt{2\gamma}}. \quad (\text{A2})$$

The claim that Equation (A2) represents an exact solution for the similarity exponent was later refuted in papers by Lazarus (1980) (with a rejoinder by Mishkin (1980)) and Yousaf (1986); see also the paper by Wang (1982). This so-called 'Landau-Stanyukovich rule' has also been recently extended by Gurovich and Fel (2009) in order to construct upper and lower bounds on the true value of the similarity exponent.

#### A.1.2. The CCW method

The Chester–Chisnell–Whitham (CCW) method is based upon the result of Chester (1954) for the motion of a shock wave in a channel with a small change in area. Chisnell (1957) first integrated Chester's result for 'freely propagating' symmetric shock waves, and Whitham (1958) produced an alternative derivation of Chisnell's result. For the case of strong shock waves, the ultimate result is an analytic formula relating the similarity exponent to the adiabatic exponent and space dimension.

It was apparently first noted by Sedov (1959) that in the neighbourhood of  $(V,C)=(0,0)$ , the solution of Equation (41) has the following limiting behaviour:

$$\lim_{V \rightarrow 0^+} C(V) = A_2 V^2, \quad (\text{A3})$$

where  $A_2$  is a constant to be determined. Since Equation (A3) automatically satisfies the boundary condition imposed upon the solution curve  $C(V)$  given by Equations (50) and (51), only the initial conditions Equations (47) and (48) remain to be utilised. In particular, imposing the latter on Equation (A3) allows for determination of the constant  $A_2$ , and Equation (A3) becomes:

$$C(V) = \frac{1}{2} \gamma (\gamma - 1) V^2. \quad (\text{A4})$$

This equation represents an approximate analytic expression for the solution curve  $C(V)$  of Equation (41). Together with the condition  $\Delta=0$  and one solution of Equations (61), (A4) provides:

$$\alpha = \frac{(\gamma + 2) \sqrt{\gamma - 1} + \gamma \sqrt{2\gamma}}{(m\gamma + 2) \sqrt{\gamma - 1} + \gamma \sqrt{2\gamma}}. \quad (\text{A5})$$

#### A.1.3. The new method

Inspired by the mathematical development of the CCW method just presented and a pseudo-limiting form of Equation (41) first derived by Hirschler and Gretler (2001) (H&G), a different approximate expression for the similarity exponent can be derived. Through the use of H&G's asymptotic treatment of Equation (41) and the initial condition given by Equations (47) and (48), an approximate

solution can be shown to hold near the singular point at  $\Delta=0$ :

$$C(V) = \alpha (\gamma - 1) V + \frac{1}{2} (1 - \gamma) V^2. \quad (\text{A6})$$

When evaluated at the singular point, Equation (A6) closes a system of three nonlinear algebraic equations with the condition  $\Delta=0$  and one solution of Equation (61). Solution of this system for  $\alpha$  is given by:

$$\alpha = \frac{\gamma (\gamma + 1) - (\gamma - 2) \sqrt{\gamma^2 - 1}}{[2 + \gamma (m - 2)] \sqrt{\gamma^2 - 1} - \gamma [\gamma (m - 2) - m]}. \quad (\text{A7})$$

Equation (A7) provides an alternative to the M&F and CCW approximations as an analytic approximation to the similarity exponent.

#### A.1.4. Discussion of results

Evaluation of Equations (A2), (A5) and (A7) for various values of  $\gamma$  and  $m$  appears in Tables A1 and A2. Plots of the relative difference  $|1 - \alpha_{\text{appr}}/\alpha_{\text{exact}}|$  for each approximation and both  $m=2$  and  $m=3$  appear in Figure A2. Several trends may be discerned from these data.

- (1) The M&F approximation underestimates  $\alpha$  for all  $\gamma$  and  $m$ .
- (2) The CCW approximation overestimates  $\alpha$  only for a small range,  $1.1 < \gamma < 2$ , for  $m=2$  and 3.
- (3) The new approximation overestimates  $\alpha$  for  $\gamma > 5/3$  for  $m=2$  and 3.
- (4) The CCW and new approximations are both more accurate than the M&F approximation for nearly all  $\gamma$  and  $m$ .
- (5) The new approximation is more accurate than the CCW approximation only for large  $\gamma$  and  $m=3$ .

As discussed in Section 3.1, an exact value for the similarity exponent is obtained by removing the  $\Delta=0$  singularity crossed by the solution of Equations (41)–(43). While all Guderley solutions employ this technique, an additional constraint is necessary in order to construct analytic approximations to  $\alpha$ . We have found that the global approach of utilising both the initial conditions Equations (47)–(48) and asymptotic solutions of Equations (41)–(43) provides analytic approximations that retain a high level of fidelity to exact semi-analytic solutions (e.g. the CCW and new approximations). The purely local M&F approximation, which employs the pressure maximum requirement (i.e. a solution of Equation (61) but *not* Equations (47)–(48)) proves less accurate. Therefore, we hypothesise that both the local–global nature and accuracy of the additional constraint largely determines the accuracy of the resulting analytic approximation.

Reasons for the accuracy difference between the CCW and new approximations for various choices of  $\gamma$  and  $m$  are not easily resolved. We hypothesise that the relative local accuracy of the approximate solutions provided by Equations (A4) and (A6) varies explicitly with  $\gamma$ . Accordingly, the accuracy of analytic  $\alpha$  calculations based upon the implementation of these approximate solutions is seen to vary in a like manner.

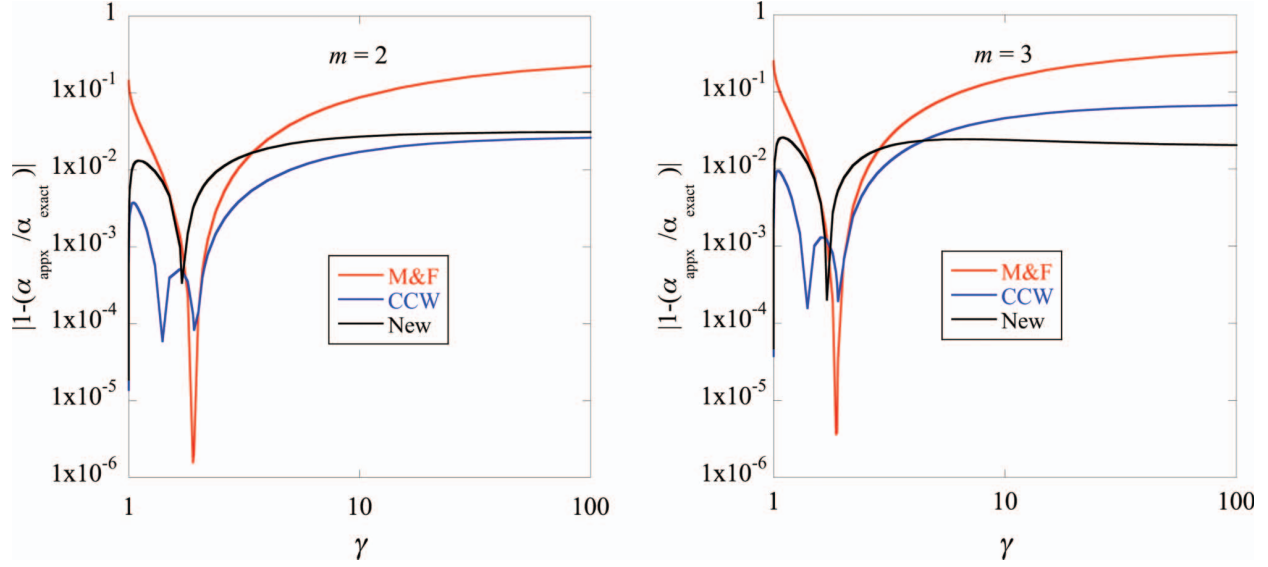


Figure A2. Relative similarity exponent differences calculated as a function of  $\gamma$  according to  $|1 - \alpha_{\text{appx}}/\alpha_{\text{exact}}|$  using the M&F, CCW, and new approximations. Left: cylindrical symmetry case ( $m=2$ ). Right: spherical symmetry case ( $m=3$ ).

Table A1. Estimates of the similarity exponent  $\alpha$  for selected values of the adiabatic exponent.

Cylindrical geometry ( $m=2$ )				
$\gamma$	Exact (Lazarus 1981)	M&F (A2)	CCW (A5)	New (A7)
1.1	0.88524806	0.84650762	0.88247182	0.87355000
1.4	0.83532320	0.82815001	0.83537259	0.82945717
5/3	0.81562490	0.81450188	0.81604351	0.81481482
1.8	0.80859994	0.80840329	0.80888426	0.80980869
2.0	0.80011235	0.8	0.8	0.80384758
3.0	0.77566662	0.76742346	0.77266101	0.78679656
5.0	0.75640105	0.72714208	0.74881559	0.77296156
10	0.74182593	0.67683841	0.72904957	0.76193475
100	0.72853594	0.56575410	0.70941536	0.75124381
$\infty$	0.72704805	0.5	0.70710678	0.75

Table A2. Estimates of the similarity exponent  $\alpha$  for selected values of the adiabatic exponent.

Spherical geometry ( $m=3$ )				
$\gamma$	Exact (Lazarus 1981)	M&F (A2)	CCW (A5)	New (A7)
1.1	0.79596980	0.73386494	0.78966404	0.77548938
1.4	0.71717450	0.70670310	0.71728743	0.70860899
5/3	0.68837682	0.68705455	0.68925126	0.6875
1.8	0.67855370	0.67842021	0.67909796	0.68040211
2.0	0.66704607	0.66666667	0.66666667	0.67202771
3.0	0.63641060	0.62261729	0.62954164	0.64852814
5.0	0.61522398	0.57126728	0.59848539	0.62994081
10	0.60104880	0.51153119	0.57362550	0.61542374
100	0.58950281	0.39446102	0.54968526	0.60159367
$\infty$	0.58828929	0.33333333	0.54691816	0.6

## Appendix 2. Calculation of cell-averaged values

Appropriate initialisation of the compressible flow code using values based on the semi-analytic Guderley solution is extremely important for proper comparison of exact and computed quantities. As the RAGE compressible flow algorithm is based on finite-volume approximations, the quantities it calculates are cell-averaged values. To initialise the code with a non-trivial flow field, one cannot simply use the point-wise flow fields that solve Equations (41)–(43), as obtained with the procedure described in Section 3.<sup>6</sup>

In order to provide input consistent with a finite-volume approach, one must evaluate cell-averaged flow fields that are consistent with the exact Guderley solution. Moreover, these cell-averaged values must be constructed from conserved quantities corresponding to those used in the governing conservation laws, namely, mass, momentum and

total energy. For the cell delimited by  $r_{\min}$  and  $r_{\max}$ , we compute the volume  $V_{\text{cell}}$ , mass  $M_{\text{cell}}$ , momentum  $MOM_{\text{cell}}$ , and total energy  $E_{\text{cell}}$  on a cell-by-cell basis. Using the notation introduced earlier, these quantities are evaluated as follows:

$$V_{\text{cell}} \equiv \frac{S_m}{m} (r_{\max}^m - r_{\min}^m), \quad (\text{A8})$$

$$M_{\text{cell}} \equiv S_m \int_{r_{\min}}^{r_{\max}} dr r^{m-1} \rho(r), \quad (\text{A9})$$

$$MOM_{\text{cell}} \equiv S_m \int_{r_{\min}}^{r_{\max}} dr r^{m-1} \rho(r) u(r), \quad (\text{A10})$$